Quantitative analysis of sideband coupling in photoinduced force microscopy

Junghoon Jahng,[1] Bongsu Kim,[2] Eun Seong Lee,[3] and Eric Olaf Potma[2]

[1]*Department of Physics and Astronomy, University of California, Irvine, California 92697, USA*
[2]*Department of Chemistry, University of California, Irvine, California 92697, USA*
[3]*Center for Nanometrology, Korea Research Institute of Standards and Science, Daejeon 304-340, South Korea*

We present a theoretical and experimental analysis of the cantilever motions detected in photoinduced force microscopy (PiFM) using the sideband coupling detection scheme. In sideband coupling, the cantilever dynamics are probed at a combination frequency of a fundamental mechanical eigenmode and the modulation frequency of the laser beam. Using this detection mode, we develop a method for reconstructing the modulated photoinduced force gradient from experimental parameters in a quantitative manner. We show evidence, both theoretically and experimentally, that the sideband coupling detection mode provides PiFM images with superior contrast compared to images obtained when detecting the cantilever motions directly at the laser modulation frequency.

DOI: 10.1103/PhysRevB.94.195407

I. INTRODUCTION

The capability of cantilever-based atomic force microscopy (AFM) to probe pN-level local forces strongly relies on the resonant mechanical motion of the cantilever beam. By detecting the tip-sample interactions at a fundamental eigenfrequency of the cantilever, the force-induced mechanical motions are amplified, which allows for a sensitive registration of forces that are at play at the nanoscale [1]. Conventional AFM methods typically use the first mechanical resonance of the cantilever beam for mapping the topography of the sample. However, the cantilever system exhibits multiple mechanical eigenmodes, and the frequencies of these modes (f_{0i}, with $i = 1, 2, \cdots$) can, in principle, be used as detection channels for probing cantilever motion.

The principle of multifrequency AFM is based on the notion that multiple frequency channels can be used simultaneously, opening up the possibility to examine different tip-sample interactions at the same time [2]. By detecting the amplitude and phase of multiple eigenmodes, the experiment can be optimized to detect, for instance, local variations in the contact difference potential [3–5] along with local mechanical measurements of material stiffness and damping [6,7]. Another example is photoinduced force microscopy (PiFM), which uses one cantilever eigenmode for registering sample topography and a second mechanical eigenmode for detecting photoinduced forces in the tip-sample junction [8–16].

In each of the frequency channels, the force-induced motion can be extracted by modulating the local force at a modulation frequency f_m and by tuning f_m close to an eigenmode frequency of the cantilever system, i.e., $f_m \approx f_{0i}$. This form of amplitude modulation detection can be labeled as the *direct mode*, because the extracted demodulated amplitude is directly related to the local force. An alternative detection scheme is the so-called *sideband coupling mode*, in which case f_m is mixed with f_i, which is a carrier frequency, and the combination frequency $f_m \pm f_i$ is detected (see Fig. 1). Unlike the direct mode, the sideband coupling mode in amplitude modulation detection is sensitive to the *gradient* of the force. Since the force gradient is often a more sensitive function of the tip-sample distance, the sideband coupling detection can produce images with sharper contrast in the

amplitude modulation AFM, compared to the direct detection mode.

Sideband coupling has been used extensively in Kelvin probe force (KPFM) microscopy [5] and in PiFM [8,9]. In both modalities, the sideband coupling scheme has been shown to yield images with improved contrast relative to direct mode detection. The sideband coupling scheme relies on the presence of a nonlinearity in the oscillating motion to enable the generation of combination frequencies. The current description of sideband coupling postulates that the origin of the nonlinearity is the force gradient in the tip-sample junction. To connect the amplitude at the sideband frequencies to the forces in the tip-sample junction, a detailed description of the force and the cantilever dynamics is required. Such descriptions are specific to the interactions at play in the junction and require a careful analysis before quantitative parameters can be extracted from the detected cantilever motions.

In this paper, we develop a quantitative theory of sideband coupling for probing force gradients detected in PiFM, in the context of multifrequency AFM. Previous theoretical descriptions of the PiFM response focused on signals detected in the direct mode [10], making it possible to deduce quantitative photoinduced forces from the cantilever motions. Here, we expand this approach to include signals detected in the sideband coupling mode, which shows a markedly different response relative to the direct mode. We compare the contrast seen in sideband coupling and direct detection modes in PiFM and explain the origins of the observed differences.

II. THEORY OF SIDEBAND COUPLING

A. Sideband coupling theory in multifrequency atomic force microscopy

The motional dynamics of a continuous beam system (cantilever-tip system) is described by the Euler-Bernoulli model. The motion of the tip apex can be approximated by a point-mass model and described by the superposition of its eigenmodes [17,18]. Because the higher eigenmodes contribute negligibly to the cantilever motion [19], for our
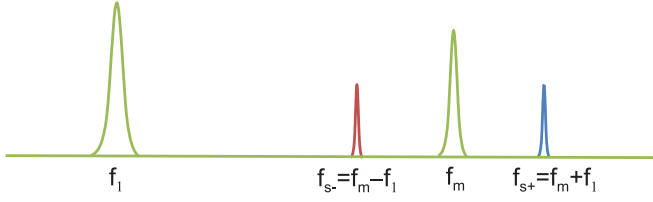
FIG. 1. Sideband coupling mechanism.

discussion here, we may assume that only the fundamental ($i = 1$) and the second mechanical resonance ($i = 2$) of the beam system are significant. The dynamics of the cantilever in two degrees of freedom can be described by [21]:

$$m\ddot{z} + b_1\dot{z} + k_1 z = F(t; z(t)) \quad (1)$$

$$m\ddot{z} + b_2\dot{z} + k_2 z = F(t; z(t)) \quad (2)$$

where m is the mass of the cantilever, $F(t; z(t))$ is the total external force including a tip-sample interaction force, and k_i and b_i are the ith spring constant and damping coefficient of the cantilever, respectively. The sideband motion is induced by coupling the modulated force gradient (f_m) with the carrier frequency (f_i). The instantaneous tip-sample distance is represented by $z(t) \simeq z_c + z_1(t) + z_m(t) + z_s(t) + O(\varepsilon)$ where z_c is the equilibrium position, z_1 is the coordinate of the carrier motion of the fundamental eigenmode, z_m describes the motion due to the modulated force, and z_s is the relevant coordinate for sideband-coupled motion (see Fig. 2). The motion of z_m and z_s can be described as the superposition of eigenmodes at their respective frequencies, given as $z_m(\omega_m) \approx \sum_{i=1}^{2} z_i(\omega_m)$ and $z_s(\omega_{s_\pm}) \approx \sum_{i=1}^{2} z_i(\omega_{s_\pm})$. Assuming that the motion is sinusoidal, the instantaneous tip-sample distance is given as

$$z(t) \approx z_c + z_1(t) + z_m(t) + z_s(t) + O(\varepsilon) \quad (3)$$

with

$$z_1(t) \approx A_1 \sin(\omega_1 t + \theta_1)$$

$$z_m(t) \approx A_{m_1} \sin\left(\omega_m t + \theta_{m_1}\right) + A_{m_2} \sin\left(\omega_m t + \theta_{m_2}\right)$$

$$z_s(t) \approx A_{s_1} \sin\left(\omega_{s_\pm} t + \theta_{s_1}\right) + A_{s_2} \sin\left(\omega_{s_\pm} t + \theta_{s_2}\right)$$

where $\omega_{s_\pm} = \omega_m \pm \omega_1$. A_{m_i} and θ_{m_i} are the amplitude and phase that are driven by the photoinduced force acting on the fundamental and second eigenmodes; A_{s_i} and θ_{s_i} are the amplitude and phase driven by the interaction responsi-
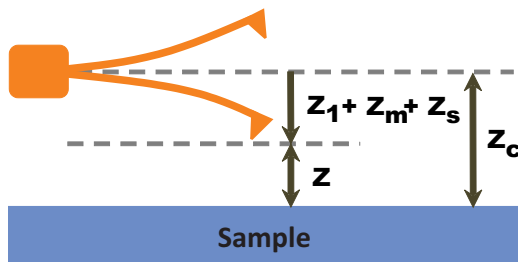

FIG. 2. Dynamic motion of a cantilever.

ble for coupling the eigenmodes. Substituting Eq. (3) into Eqs. (1) and (2) by multiplying both sides of the resulting equation by $\sin(\omega_j t + \theta_j)$ and $\cos(\omega_j t + \theta_j)$, followed by an integration over the oscillation period, the following general relations for the amplitude and phase of the motions are obtained:

$$\left(k_i - m\omega_j^2\right)\frac{A_j}{2} = \frac{1}{T}\int_0^T F(t; z(t))\sin(\omega_j t + \theta_j)dt \quad (4)$$

$$\frac{b_i \omega_j A_j}{2} = \frac{1}{T}\int_0^T F(t; z(t))\cos(\omega_j t + \theta_j)dt \quad (5)$$

where $i = 1,2$, $j = 1, m_i, s_{i\pm}$. Equations (4) and (5) are the general expressions of our sideband coupling theory in multifrequency atomic force microscopy. If the form of $F(t)$ is known, the amplitudes $A_1, A_{m_i}, A_{s_{i\pm}}$ and the phase shifts $\theta_1, \theta_{m_i}, \theta_{s_{i\pm}}$ can be calculated through numerical integration. In the next subsection, we will consider the small oscillation limit and apply the sideband coupling theory to the case where photoinduced forces are detected.

B. Small oscillation limit

Under the assumption that the oscillation is sufficiently small, Eqs. (4) and (5) can be analytically solved by regarding the sideband motion z_s as a perturbation. Note that this small oscillation approximation is equivalent to the first-order approximation to the general motion of the cantilever system [20]. The total external force can be expanded at the equilibrium position z_c as follows:

$$F(t; z(t)) \approx F(z_c) + \left(\frac{\partial F}{\partial z}\right)_{z_c}(z - z_c) + \dots \quad (6)$$

We assume that the higher order coupling terms (second order and higher) can be ignored in the small oscillation limit. In PiFM with sideband mode detection, we modulate the fundamental eigenmode of the cantilever for tracking the topography and modulate the optical force at the angular frequency ω_m. Therefore, the total external force can be written as:

$$F(t; z(t)) = F_1\cos(\omega_1 t) + F_{int}(z) + F_{pif}^{DC}(z)$$
$$+ F_{pif}^{AC}(z)\cos(\omega_m t + \theta_{pif}), \quad (7)$$

where F_1 is the driving force for the fundamental resonance, and F_{int} is a mechanical tip-sample interaction force that can be generally described as the sum of a conservative and a nonconservative force: $F_{int}(z) = F_c(z) - \Gamma(z)\dot{z}$ [21]. Such a form of the force provides a good description of the energy dissipation of the cantilever [22,23]. In the small oscillation limit, nonvelocity dependent effects, such has the hysteresis effect, can be assumed to be small [24]. The photoinduced force contributes the third and fourth term on the righthand side of Eq. (7), and is given as $F_{pif}^{DC} + F_{pif}^{AC}\cos(\omega_m t + \theta_{pif})$ [25]. The origin of the sideband signal derives from the product of the carrier motion and the modulated force. Inserting Eq. (3) and Eq. (7) into Eq. (6), then the external force induced by sideband is explicitly obtained as follows from the second

term of Eq. (6):

$$
\begin{aligned}
F_{\text{side}} &= \left(\frac{\partial F}{\partial z} \right)_{z_c} z_1(t) \\
&= \left(\frac{\partial F_{\text{pif}}^{AC}}{\partial z} \right)_{z_c} \cos(\omega_m t + \theta_{\text{pif}}) A_1 \sin(\omega_1 t + \theta_1) \\
&= \pm \left(\frac{\partial F_{\text{pif}}^{AC}}{\partial z} \right)_{z_c} \frac{A_1}{2} \sin(\omega_{s_\pm} t + \theta_{\text{pif}} \pm \theta_1) \\
&= F(\omega_{s_+}) + F(\omega_{s_-}),
\end{aligned}
\tag{8}
$$

where $\omega_{s_\pm} = \omega_m \pm \omega_1$ are the sum and difference frequencies at which the sideband coupled signal is detected. In the remainder of this paper, we will choose ω_{s_-} for our sideband detection. By setting the sideband frequency to coincide with the second resonance frequency, $\omega_s \equiv \omega_{s_-} = \omega_2$, the sideband motion is amplified by the second eigenmode. For abbreviated notation, we will write the gradient of the photoinduced force as $k_{\text{pif}}^{AC} = \left(\frac{\partial F_{\text{pif}}^{AC}}{\partial z} \right)_{z_c}$.

When we consider the sideband motion as a perturbed motion, by substituting Eq. (6) into the integral forms of Eqs. (4) and (5), the integral can be evaluated over the period $T = 2\pi p_1/\omega_1 = 2\pi p_s/\omega_s = 2\pi p_m/\omega_m$ in which the motion $z(t)$ is periodic. The intermediate steps in this calculation are explained in the Appendix. In the resulting equations, the force gradient acts as a perturbation that alters the amplitude and frequency of the carrier motion. For the unperturbed solution, the following general relations for the amplitude and the phase of the carrier and the sideband motion are obtained:

$$
A_1(\omega_1) = G_1(\omega_1) F_1 \tag{9}
$$

$$
A_s(\omega_s) = G_2(\omega_s) \frac{k_{\text{pif}}^{AC}(z_c)}{2} A_1 \tag{10}
$$

with the transfer function

$$
G_i(\omega_j) = \frac{1}{\sqrt{m^2 \left(\omega_i'^2 - \omega_j^2 \right)^2 + (b_i' \omega_j)^2}}, \tag{11}
$$

where $\omega_i' = \sqrt{(k_i - \left(\frac{\partial \bar{F}_c}{\partial z} \right)_{z_c})/m}$ accounts for the frequency shift induced by the force gradient, $\bar{F}_c = F_c + F_{\text{pif}}^{DC}$ is the effective conservative force, and $b_i' = b_i + \Gamma(z_c)$ is an effective damping parameter. Equation (9) is the unperturbed solution of the carrier motion. Equation (10) is the first order perturbation solution due to the presence of the modulated force. Note that the expressions (9) and (10) are similar to the equations found in prior work [5]. Here we advance previous work by including damping explicitly in the transfer function and by using amplitude and phase information of the first eigenmode for calculating the transfer function of the cantilever's second eigenmode.

The amplitude of the sideband motion A_s is proportional to the force gradient of the photoinduced force rather than to the photoinduced force itself. For comparison, the amplitude of the photoinduced force, which is probed in the *direct* detection mode, is given as [10]:

$$
A_d(\omega_2) = G_2(\omega_2) F_{\text{pif}}^{AC}(z_c). \tag{12}
$$

Because the detected amplitude in the direct mode is directly related to F_{pif}^{AC}, the signal contains both localized (attractive) and nonlocalized (repulsive) force contributions [14]. On the other hand, the sideband mode is related to the force gradient of the photoinduced force, k_{pif}^{AC}. Therefore, since the gradient of localized force contributions is much higher than the gradient of the slowly varying nonlocalized forces, the sideband is much more sensitive to localized tip-sample interactions. The reduced spatial scale at which these interactions are prominent gives rise to a high spatial resolution and improved contrast compared to what is seen in the direct detection mode. We will compare contrast attained in the sideband and direct mode in Sec. V based on both simulation and experimental results. In the next section, we will develop a method for reconstructing the modulated force gradient from the cantilever motion.

C. Reconstruction of distance-dependent force

The amplitude and phase of the carrier motion detected in the sideband mode are experimentally accessible quantities. We next describe an analytical method to relate the experimental observables to the force gradients present in the tip-sample junction. Evaluating the integrals in Eqs. (4) and (5) and using Eq. (6), the force gradients of the photoinduced force and the mechanical interaction force can be expressed as:

$$
\bar{k}_c(z) = -\frac{F_1}{A_1(z)} \sin \theta_1(z) + \left(k_1 - m \omega_1^2 \right) \tag{13}
$$

$$
\Gamma(z) = \frac{F_1}{A_1(z) \omega_1} \cos \theta_1(z) - b_1 \tag{14}
$$

$$
\left| k_{\text{pif}}^{AC}(z) \right| = \frac{A_s(z)}{A_1(z)} \frac{2}{G_2(\omega_s)} \tag{15}
$$

with $b_2' = b_2 + \Gamma(z)$, $\bar{k}_c(z) = \left(\frac{\partial \bar{F}_c}{\partial z} \right)_{z_c}$ and $\omega_2' = \sqrt{(k_2 - \left(\frac{\partial \bar{F}_c}{\partial z} \right)_z)/m}$ where $\bar{F}_c = F_c + F_{\text{pif}}^{DC}$. The intermediate steps in deducing these equations can be found in the Appendix. The formalism outlined by Eqs. (13)–(15) makes it possible to reconstruct the distance dependent force gradient of the mechanical and photoinduced force from the experimentally accessible parameters A_1, A_s, and θ_1. Note that Eq. (15) describes, in general, any applied force gradient that introduces sideband motion in the cantilever system at the sideband frequency $f_{s_\pm} = f_m \pm f_1$. Note also that we have assumed that the effective force gradient acts on both the first and the second mode of the cantilever.

III. AMPLITUDE-DISTANCE SIMULATIONS

We first study the general trends of the cantilever dynamics in the presence of both mechanical and photoinduced forces by using Eqs. (9) and (10). For this purpose, it is required to choose a functional form for the forces F_{int} and F_{pif}. There are numerous formulations for conservative (F_c) and nonconservative (F_{nc}) forces [1,26–28]. In this simulation, we will consider the simplest case in which the mechanical tip-sample interaction force can be described by an attractive van der Waals type conservative force and the photoinduced forces are the attractive localized gradient force

F_g and the repulsive scattering force F_{sc} [10] are modeled as:

$$F_{\text{int}}(z) = -\frac{HR}{6z^2} \qquad (16)$$

$$F_{\text{pif}}(z) = -\frac{\beta}{z^4} + F_{sc}, \qquad (17)$$

where H is the Hamaker constant, R is the tip radius, and z is the distance between the tip's apex and the sample surface. The magnitude of the photoinduced gradient force depends on the β parameter, which is defined as $\beta = 3\,\text{Re}\{\alpha_t^* \alpha_p\}E_{0z}^2/2\pi\varepsilon_0$, where E_{0z} is the z component of the incident field, and α_t and α_p are the complex polarizability of the tip and the molecule, respectively [29]. The scattering force F_{sc} is regarded as a constant in the near-field region.

Figure 3 shows the distance dependent (a) amplitude and (b) phase curves of the fundamental resonance and the amplitude of the sideband mode (c) with the chosen simulation parameters [30]. Simulations are shown for two settings of the photoinduced force, where the β parameter for the red solid curve is ten times higher than for the black solid curve. In Fig. 3(d), the gradient of the photoinduced force is plotted for the two different settings of the β parameter, using Eq. (17) for the functional form of the distance-dependent force. The green squares (β) and blue dots (10β) represent the reconstructed force gradient by using Eq. (15) with the plotted A_1, A_s, and θ_1, respectively. As is clear from the figure, the overlap of the reconstructed force gradient with the calculated force gradient is excellent, underlining that the reconstruction formalism accurately reproduces the active force. Note that, unlike direct mode detection [10], the sideband coupling detection mode is not sensitive to the constant scattering force, which is reflected in the absence of scattering force effects in the distance dependence of k_{pif}.

When the tip approaches the sample surface, the amplitude at the carrier frequency decreases because the gradient of the conservative force increases, which leads to a change in the frequency shift ω_i' [Fig. 3(a)]. When the localized force is increased by 10 times (red solid line), the gradient of the DC component of the photoinduced force (F_{pif}^{DC}) also contributes to ω_i', and the amplitude (and phase) at the carrier frequency are further reduced at shorter tip-sample distances [Figs. 3(a) and 3(b)]. This effect is related to the *optical force artifact* known in scattering near-field optical microscopy [31,32].

Unlike the amplitude at the carrier frequency (A_1), the amplitude at the sideband frequency (A_s) is sensitive to the *modulated* force gradient of the photoinduced force, k_{pif}^{AC}. In Fig. 3(c), A_s is seen to go through a maximum as the tip approaches the sample. For the black solid line, the maximum appears near $z \approx 1$ nm for the chosen beta prefactor [30]. The magnitude and the width of the peak is dependent on β, which in turn is related to the effective polarizabilities of the tip and the sample. By increasing the localized force by 10 times (red solid line), the AC force gradient enhances the magnitude and width of the peak in the amplitude-distance curve. In addition, the maximum of the curve has shifted to $z \approx 1.4$ nm. The simulation thus shows that A_s is very sensitive to k_{pif}^{AC}.
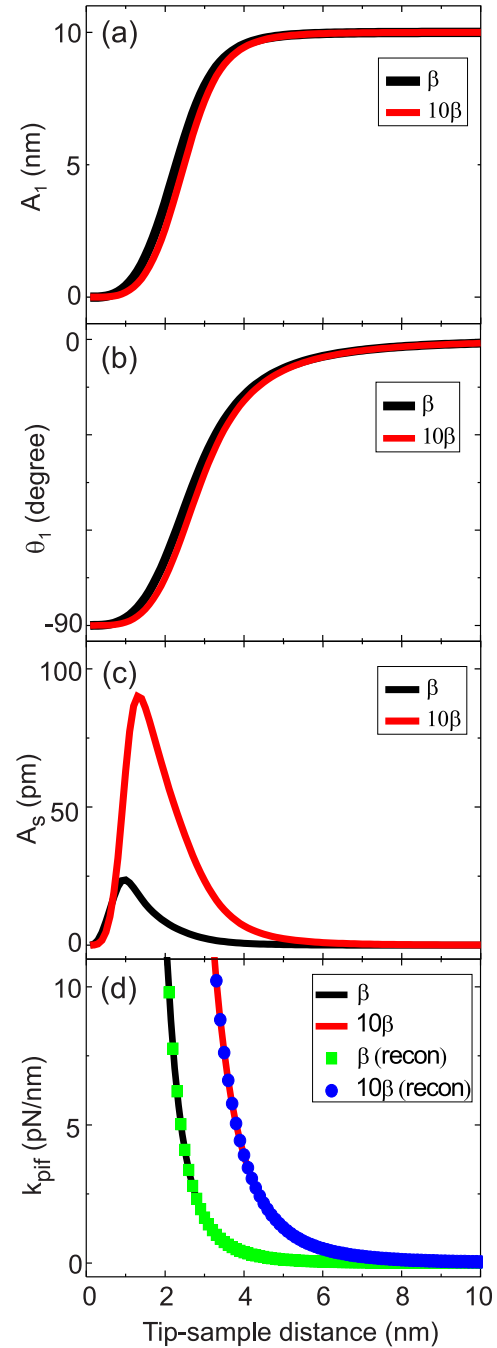
FIG. 3. (a) Amplitude and (b) phase curves of the fundamental resonance. (c) Amplitude of the sideband mode and (d) modulated photoinduced force gradient with respect to tip-sample distance and the beta prefactors: β (black solid line) and $10\,\beta$ (red solid line). The reconstructed force gradients obtained with Eq. (15), and by using the above A_1, A_s and θ_1, are plotted with green squares (β) and blue circular ($10\,\beta$) dots. [30].

IV. EXPERIMENT

A. Sample materials

Two test samples are used in this study. The first sample consists of gold nanowires patterned on a 0.17 mm thick borosilicate coverslip. The nanowires are fabricated by the lithographically patterned nanowire electrodeposition

FIG. 4. Sketch of the photoinduced force microscope.

technique [33]. The resulting nanowires exhibit an average width of 120 nm and an average height of 40 nm, whereas the length of the nanowires extends over millimeters. The second sample is a borosilicate coverslip with deposited nanoclusters of silicon 2,3-naphthalocyanine bis(trihexylsilyloxide) (SiNc) (Sigma-Aldrich). The samples are prepared by spincasting a concentrated solution of SiNc in toluene onto a plasma-cleaned coverslip. After evaporation of the solvent, a distribution of nanoscale SiNc aggregates is seen, varying in size from several micrometers to less than 10 nm in diameter.

B. Light source

The experiments are carried out with a femtosecond light source (MaiTai, Spectra-Physics), which delivers a 80 MHz, 200 fs pulse train. The average power of the laser beam at the sample plane is around 50 μW to 90 μW at 809 nm wavelength for both samples. The laser light is amplitude modulated by an acousto-optic modulator at a frequency $f_m = f_s + f_1$ with $f_s = f_{02}$. The beam, which is linearly (x) polarized, is expanded with a beam expander to a diameter of $\sim$5 mm and steered to an optical microscope. A schematic of the optical layout is given in Fig. 4.

C. Atomic force microscope

A custom-modified atomic force microscope (Molecular Vista–VistaScope) is used for the PiFM experiments. A simplified scheme of the force detection is included in Fig. 4. The system consists of an inverted optical microscope equipped with a NA = 1.40 oil immersion objective, a sample stage

scanner, an AFM scan head and transmission and reflection optics for sample inspection. The incident laser light is focused by the microscope objective to produce a diffraction-limited focal spot at the sample plane. The focal field thus produced contains significant portions of y-polarized and z-polarized light. To optimize the PiFM contrast, the tip is positioned at the location of maximum z-polarized light in the focal spot, making the measurement sensitive to the z-directed localized forces [14].

We have measured the free oscillation resonance curve (amplitude versus frequency) and the DC deflection to calibrate the sensitivity of the cantilever and fitted the free oscillation carrier amplitude by using Eq. (9), which is obtained at 10μm above the sample without applying the laser beam. We measured the sensitivity as 5.13 mV/nm and the free oscillation amplitude A_{01} as 194.66 mV. This yields a calibrated free oscillation amplitude of $194.66/5.13 = 38$ nm. By fitting the free oscillation resonance curve, we also extracted the other mechanical parameters of the cantilever such as its quality factor. PiFM experiments are carried out with a 30 nm diameter gold coated silicon tip (ACLGG, App-Nano Inc.). The measured mechanical properties of this cantilever are $k_1 = 48$ N/m, $f_{01} = 177.7$ kHz, $Q_1 = 676$, $k_2 = 1992.3$ N/m, $f_{02} = 1094.6$ kHz, and $Q_2 = 654$.

The topographic and photoinduced force images are acquired simultaneously. This is achieved by demodulating the tip response at f_{01} to retrieve the topography image and at f_s to retrieve the photoinduced force image. The laser modulation frequency was set to $f_m = f_s + f_1$ for photoinduced force measurements, coinciding the sideband (difference) frequency with the second mechanical resonance of the cantilever $f_s = f_{02}$ to amplify the A_s signal. Because the demodulation frequency is at a relatively high frequency (1094.6 kHz), thermal noise contributions play only a minor role.

The minimum detectable force and the thermal noise amplitude of each eigenmode of a cantilever are given as $F_{min_i} = \sqrt{4 k_i k_B T B / Q_i \omega_{0i}}$ and $N_i = \sqrt{4 k_B T Q_i B / \omega_{0i} k_i}$, where B is the bandwidth of a measurement and i is the ith eigenmode [34]. For the second resonance with $B = 100$ Hz and $T = 300$ K, the minimum detectable force and the thermal noise amplitude are 1.03×10^{-13} N and 1.45×10^{-12} m for the fundamental resonance and 8.57×10^{-13} N and 2.81×10^{-13} m for the second mechanical resonance, respectively.

V. CONTRAST ANALYSIS OF SIDEBAND COUPLING IN PIFM

We next apply the developed formalism to experimentally obtained amplitude-distance measurements and show that quantitative force information can be extracted from signals detected through the sideband coupling scheme. We first inspect the gold nanowire sample, where we measure the distance-dependent PiFM signal between the gold-coated tip and the gold surface of the nanowire. The bare glass surface next to the nanowire is used as a reference. Figure 5 shows the (a) amplitude and the (b) phase of the fundamental resonance of the cantilever when operated at a free oscillation amplitude $A_{01} = 38$ nm, recorded when the tip is parked over the glass (black) and gold nanowire (red). The blue region is the hard contact region where the cantilever beam is mechanically
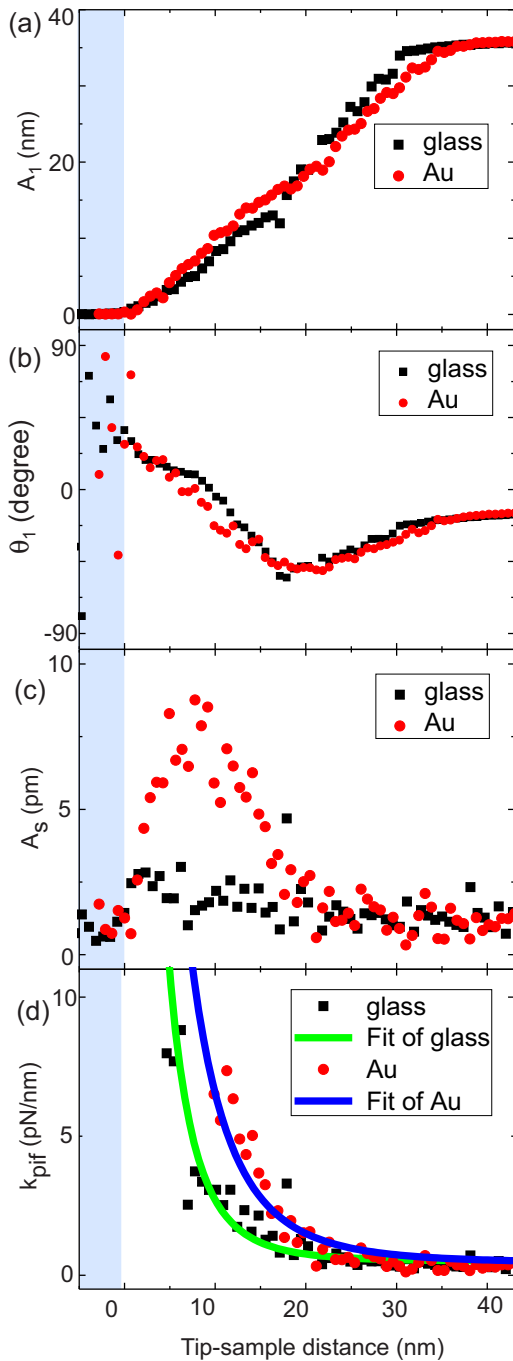
FIG. 5. (a) Amplitude and (b) phase curves of the fundamental resonance. (c) Amplitude of the sideband mode with respect to tip-sample distance. Black square dots correspond to the glass surface and the red circular dots denote the measurement on gold. (d) Reconstructed force gradients obtained with Eq. (15), by using the above A_1, A_s, and θ_1, are plotted as black square (glass) and red circular (gold) dots. The curves are fitted by the gradient of Eq. (17) for glass (green solid line) and gold (blue solid line).

bent. The latter region corresponds to the hard contact mode where the thermal expansion force is an important contributor to the measurement [35]. Here, we are mainly concerned with the region accessible with the noncontact/tapping mode of the AFM, a region where photoinduced forces are

important. As is evident from the figure, the difference between the curves obtained over the glass and the gold surface is very small. These observations corroborate the trends seen in the simulations of Figs. 3(a) and 3(b), emphasizing that the photoinduced force effects are minimal in the A_1 and θ_1 detection channels.

On the other hand, the A_s detection channel clearly shows a difference between the measurement for glass and for gold, as evidenced in Fig. 5(c). For the measurement performed over the gold surface, the sideband amplitude is maximized at a distance of $z \approx 7.5$ nm from the material, while falling off for larger tip-sample distances. When the same measurement is conducted over glass, the amplitude at the sideband frequency is significantly less, showing a shallow maximum near $z \approx 2$ nm. These general features are similar to what is predicted by the theory calculations presented in Fig. 3(c). The increased A_s for gold is expected because gold exhibits a much higher polarizability than glass, corresponding to a higher β value.

In order to extract quantitative information from the sideband amplitude distance curve, we use our reconstruction formalism to compute the field gradient (k_{pif}^{AC}). The results are shown in Fig. 5(d). The blue and green solid lines are fits based on the gradient of the force presented in Eq. (17) using the β prefactor as a fitting parameter. Using this approach, we find β as 4.7×10^{-41} N m^4 for gold and 5.2×10^{-42} N m^4 for glass. The beta value depends on the field enhancement, material polarizability, and the total beam intensity. The different β values thus reflect the difference in the effective polarizability of the materials under the tip, with a higher effective polarizability for gold relative to glass.

As discussed above, the sideband coupling detection mode is sensitive to the gradient of the photoinduced force, whereas the direct mode is sensitive to the photoinduced force itself. This implies that PiFM images taken in the sideband coupling mode may appear very different from the images obtained in the direct mode. A direct comparison is presented in Fig. 6, which shows a measurement on SiNc nanoclusters on glass. In panel (a), the PiFM response from a nanocluster is shown as a function of laser intensity for both the sideband coupling mode (pink squares) and the direct mode (black dots). For this measurement, the tip was parked 10 nm above a selected nanocluster. We observe a marked difference in the laser intensity dependence between the two detection modes. A higher laser intensity corresponds to a higher β value and thus to a higher F_{pif}^{AC}. Using the expression of the photoinduced force, Eq. (17), we can simulate the amplitude of the sideband coupling mode and the direct mode by employing equations (10) and (12), respectively.

The most notable difference between the curves is that the curve for the sideband coupling mode goes through a maximum, while the curve for the direct mode saturates at higher intensities of the laser light. This difference is explained by the different expressions for A_s and A_d. For a given magnitude of the photoinduced force, A_d is proportional to the AC force through the transfer function which is inversely proportional to the DC force gradient. The expression for A_d depends on β as $C_1\beta/\sqrt{C_2\beta^2 + C_3}$, which is simplified from Eq. (12) and where C_i are constants. This functional form shows that A_d saturates in the limit of high β values. However, the sideband amplitude A_s shows a more complex dependence
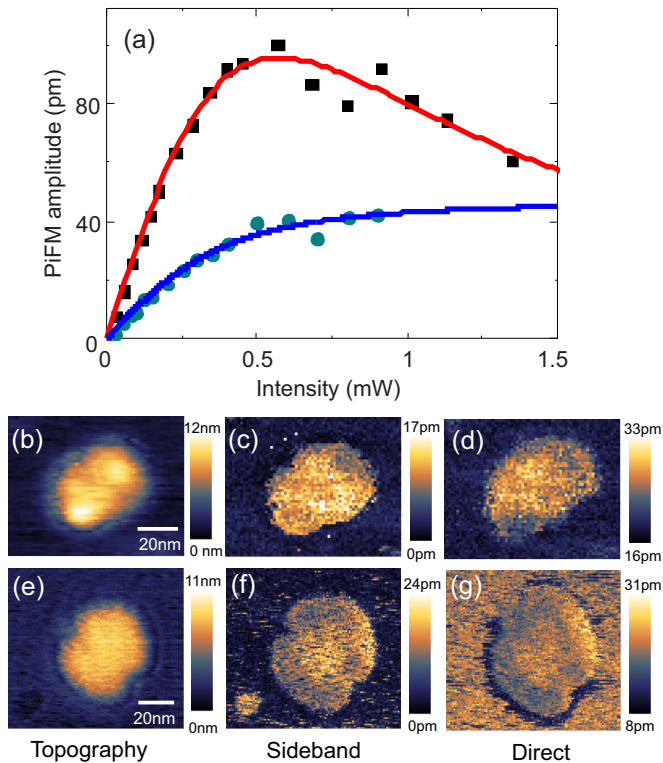
FIG. 6. (a) Laser intensity dependence of the sideband coupled mode and the direct mode. Experimental sideband coupled signal is indicated by black square dots and the simulation based on Eq. (10) by the red solid line. Experimental direct modulation signal is shown by the green circular dots and simulation based on Eq. (12) by the blue solid line. The tip-sample distance is ∼10 nm. Images of SiNc clusters are shown for the topography (b) and (e), PiFM sideband (c) and (f), and PiFM direct modulation (d) and (g). The tip-sample distance is 10 nm (top row) and 26 nm (bottom row).

on β. A_s can be simplified and rewritten in terms of β as $c_1\beta/\sqrt{c_2\beta^4 + c_3\beta^2 + c_4}$, where c_i are constants. This form shows that A_s exhibits a maximum as a function of β. The result of the simulation is shown by the solid lines in Fig. 6(a), which reproduces the experimentally obtained data very well.

Figure 6(a) also contains clues toward the expected differences in PiFM images, detected in either the sideband coupling mode or the direct mode. It can be seen that for smaller β values (lower laser power), the slope of the PiFM response in the sideband coupling mode is steeper than in the direct mode. This steeper β dependence translates into an enhanced sensitivity of the sideband coupling mode. We thus expect to see higher contrast in sideband coupling detected PiFM images. Figure 6(b) shows a topography image of a SiNc nanocluster. The corresponding images obtained with the modulation frequency set to $f_m = f_s + f_{01}$, where $f_s = f_{02}$ (sideband frequency), and to $f_m = f_{02}$ (direct frequency) are shown in panels (c) and (d), respectively. The images are obtained at a tip-sample distance of 10 nm. It can be seen that the contrast in the sideband coupling mode is indeed noticeably better, with sharper defined features especially at the edges of the nanocluster.

Besides the steeper β dependence, the sideband coupling also suppresses contributions originating from the scattering force. Since the scattering force is largely insensitive to the polarizability of the sample (molecule), it gives rise to a background signal that reduces the contrast in PiFM images. The effect of the scattering force can be significant at larger tip-sample distances, where the magnitude of the gradient force is reduced. In Fig. 6(e), the topography of another SiNc nanocluster is shown, along with the corresponding PiFM images obtained in the sideband coupling mode (f) and the direct mode (g), now recorded at a tip-sample distance of 26 nm. It is evident that the contrast in panel (g) is compromised. The much lower gradient force is overwhelmed by the constant scattering force, producing an image with limited contrast. In the sideband coupling mode, however, the scattering force is suppressed, and the gradient force, though weak, can still be discerned. This example illustrates that the sideband coupling mode offers enhanced sensitivity to the gradient force in scenarios where the scattering force may otherwise dominate the PiFM response.

VI. DISCUSSION AND CONCLUSION

The existence of cantilever motions at sideband frequencies implies the presence of nonlinearities that enable the mixing two frequencies at which the system is driven. The cantilever beam is inherently nonlinear and is thus capable of synthesizing motions at frequencies that are combinations of input frequencies [17,18,36,37]. However, the manifestation of sideband motions is evident only when the beam is driven at large oscillation amplitudes, typically over a few hundred nanometers. For much smaller oscillation amplitudes, such as used in PiFM imaging applications with relatively stiff cantilever beams, the intrinsic nonlinearity of the system does not generate significant sideband motions. In this limit, the probe is considered a linear harmonic oscillator [18,20], and intrinsic nonlinearities can be ignored. In the linear oscillator regime, the origin of nonlinearities is found in the force interactions experienced by the cantilevered tip [38,39]. In particular, the presence of a force gradient offers a mechanism for mixing two driving frequencies, generating a response at the respective sum and difference frequencies. The amplitude of the sideband oscillation thus scales with the magnitude of the force gradient experienced by the tip.

The sensitivity of the sideband oscillations to the force gradients in the tip-sample junction has been long recognized and utilized in Kelvin probe force microscopy and recently in PiFM microscopy. In PiFM, where the sample is illuminated with a modulated laser beam, the sideband coupling detection scheme sensitively probes the field gradient of the optically induced force in the tip-sample junction. The photoinduced force contributes both a gradient force and a scattering force, and since the tip-sample interactions are reflected mostly in the gradient force, rejection of the scattering force is of great relevance. By suppressing the scattering force, the sideband coupling detection scheme displays a unique sensitivity to the sample's polarizability, enabling spectroscopic imaging of nanoscopic entities [14]. Although the favorable attributes of sideband coupling detection are known [8,9], a general theoretical description explaining the origin of the PiFM imaging contrast in this mode has not been previously discussed. The work discussed here presents a fully consistent theoretical

framework for quantitatively analyzing and predicting PiFM signals detected in the sideband coupling mode.

Our description considers the cantilever motions at multiple frequencies and interprets their amplitudes in the context of mechanical and optical forces and their gradients in the tip-sample junction. The formalism considers the mixing between oscillations at all the relevant driving frequencies, and our theory confirms that the sideband frequencies observed in PiFM find their origin in the gradient of the photoinduced force. By tuning the sideband mixing frequency to a mechanical resonance of the cantilever system, the amplitude at the sideband frequencies can be significantly amplified, thus enhancing the sensitivity of the technique to the modulated gradient of F_{pif} or k_{pif}^{AC} for short.

A second attribute of the formalism developed here is that quantitative values for k_{pif}^{AC} can be extracted from experimental measurements of the oscillation amplitudes of the cantilever at the sideband frequency. Using A_1, θ_1, and A_s as input parameters, we predict values for k_{pif}^{AC} that coincide with reasonable estimates of the photoinduced forces in the junction. For instance, the reconstruction method enables us to directly compare the theoretically predicted distance dependence of k_{pif}^{AC} with experimentally obtained tip-sample distance measurements [Fig. 5(d)]. This ability renders sideband detected PiFM a quantitative imaging technique.

All the main signatures in the distance dependence of the amplitude and phase at the fundamental and sideband frequencies, obtained from experiments, are reproduced in the sideband coupling theory discussed in this paper. In particular, we find a characteristic maximum of the sideband amplitude as a function of tip-sample distance, which depends on the magnitude of β, the prefactor included in k_{pif}^{AC}. Another experimental observable, the PiFM amplitude as a function of β, obtained by increasing the laser intensity, is also correctly predicted by our theory. We find that the β dependence of the amplitude detected in the sideband coupled mode is markedly different from the amplitude registered in the direct mode. In the low intensity limit, which coincides with typical experimental conditions, we observe that the sideband amplitude displays a higher sensitivity to β compared to the amplitude in the direct mode. This enhanced sensitivity is a key factor that explains why images obtained in the sideband coupling mode appear sharper and with more detail.

Sideband coupling detection is not limited to PiFM or Kelvin probe microscopy. The sideband principle has also been applied to enhance the contrast in bimodal AFM to probe sample elasticity and damping [38]. In frequency modulated Kelvin probe microscopy, sideband coupling detection has been used in a multifrequency AFM approach to extract the contact potential as well as the topography [3,40]. The theory developed in this work is general and can be applied to the latter examples of sideband detected AFM as well. We expect that beyond its use in PiFM, the current theory and reconstruction method may aid other scan probe techniques in extracting quantitative information from experiments.

APPENDIX: MODELING DETAILS

In the experiment, the sideband frequency is set to match the frequency of the second mechanical resonance of the cantilever system. To simplify the calculation, we choose ω_{s_-} for the sideband detection by setting it as $\omega_s = \omega_{s_-} = \omega_m - \omega_1 = \omega_2 \approx 6.27\omega_1$. Because ω_{s_-} is far removed from the first mechanical resonance, we can approximate the amplitude of the sideband mode as $A_s \approx A_{s_{2-}} \gg A_{s_{1-}}$. By considering the above approximation, the integral equations for the carrier and sideband motions are rewritten as:

$$\left(k_1 - m\omega_1^2\right)\frac{A_1}{2} = \frac{1}{T}\int_0^T F(t)\sin(\omega_1 t + \theta_1)dt \quad \text{(A1)}$$

$$\frac{b_1\omega_1 A_1}{2} = \frac{1}{T}\int_0^T F(t)\cos(\omega_1 t + \theta_1)dt \quad \text{(A2)}$$

$$\left(k_2 - m\omega_s^2\right)\frac{A_s}{2} = \frac{1}{T}\int_0^T F(t)\sin(\omega_s t + \theta_s)dt \quad \text{(A3)}$$

$$\frac{b_2\omega_s A_s}{2} = \frac{1}{T}\int_0^T F(t)\cos(\omega_s t + \theta_s)dt. \quad \text{(A4)}$$

The carrier motion can be obtained by calculating Eqs. (A1) and (A2). The sideband motion can be obtained by calculating Eqs. (A3) and (A4). The integration can be performed over the period $T = 2\pi p_1/\omega_1 = 2\pi p_s/\omega_s = 2\pi p_m/\omega_m$ in which the signal $z(t)$ is periodic. The eigenmode frequencies, ω_1, ω_s, and ω_m, are required to be commensurable; i.e., $\omega_1/\omega_s = p_1/p_s$, $\omega_1/\omega_m = p_1/p_m$ and $\omega_s/\omega_m = p_s/p_m$, where p_1, p_m, and p_s are integers. This is always possible with high accuracy such as $p_1 = 15, p_s = 94$ and $p_m = 109$ for $\omega_s = \omega_2 = 6.27\omega_1$ and $\omega_m = 7.27\omega_1$. The physical meaning of $p_1, p_s,$ and p_m is to increase the measuring time. The total force in PiFM is given as

$$\begin{aligned} F(t;z(t)) = \ &F_1\cos(\omega_1 t) + F_{\mathrm{int}} + F_{\mathrm{pif}}^{DC}(z) \\ &+ F_{\mathrm{pif}}^{AC}(z)\cos(\omega_m t + \theta_m) \end{aligned} \quad \text{(A5)}$$

where $F_{\mathrm{int}} = F_c(z) - \Gamma(z)\dot{z}$. With a small oscillation approximation, the total force can be expanded as:

$$F(t;z(t)) \approx F(z_c) + \left(\frac{\partial F}{\partial z}\right)_{z_c}(z - z_c) + \cdots \quad \text{(A6)}$$

where $z(t) \approx z_c + z_1(t) + z_m(t) + z_s(t)$. Substituting Eq. (A5) into Eq. (A6), by considering the higher order terms are sufficiently small, the total force terms are rewritten as:

$$F_1\cos(\omega_1 t) = F_1\cos(\omega_1 t) \quad \text{(A7)}$$

$$F_c(z) \approx F_c(z_c) + \left(\frac{\partial F_c}{\partial z}\right)_{z_c}(z_1 + z_m + z_s) \quad \text{(A8)}$$

$$\Gamma(z)\dot{z} \approx \left(\Gamma(z_c) + \left(\frac{\partial \Gamma(z)}{\partial z}\right)_{z_c}(z_1 + z_m + z_s)\right)\dot{z} \quad \text{(A9)}$$

$$F_{\mathrm{pif}}^{DC}(z) \approx F_{\mathrm{pif}}^{DC}(z_c) + \left(\frac{\partial F_{\mathrm{pif}}^{DC}}{\partial z}\right)_{z_c}(z_1 + z_m + z_s) \quad \text{(A10)}$$

$$F_{\text{pif}}^{AC}(z)\cos(\omega_m t + \theta_m) \approx F_{\text{pif}}^{AC}(z_c)\cos(\omega_m t + \theta_m)$$

$$+ \left(\frac{\partial F_{\text{pif}}^{AC}}{\partial z}\right)_{z_c}(z_1 + z_m + z_s)\cos(\omega_m t + \theta_m). \quad \text{(A11)}$$

When we set $\omega_s = \omega_m - \omega_1 = \omega_2$, the second term in Eq. (A11) gives the coupled response between the motions through the modulated photoinduced force gradient. The sideband force is explicitly derived from this coupled response as below:

$$\left(\frac{\partial F_{\text{pif}}^{AC}}{\partial z}\right)_{z_c}\cos(\omega_m t + \theta_m)z_1$$

$$= \left(\frac{\partial F_{\text{pif}}^{AC}}{\partial z}\right)_{z_c}\cos(\omega_m t + \theta_m)A_1\sin(\omega_1 t + \theta_1)$$

$$= \left(\frac{\partial F_{\text{pif}}^{AC}}{\partial z}\right)_{z_c}\frac{A_1}{2}\sin((\omega_m + \omega_1)t + \theta_m + \theta_1)$$

$$- \left(\frac{\partial F_{\text{pif}}^{AC}}{\partial z}\right)_{z_c}\frac{A_1}{2}\sin(\omega_s t + \theta_m - \theta_1) \quad \text{(A12)}$$

where $\omega_s \equiv \omega_m - \omega_1$. The first term in Eq. (A12) is the right sideband force ω_{s_+} and the second term is the left sideband force ω_{s_-}. Because we will choose the left sideband for our detection, the sideband frequency is given as $\omega_s \equiv \omega_{s_-} = \omega_2$. When we consider the sideband motion as a perturbation, the total motion can be described as:

$$z(t) \approx z^{(0)} + z^{(1)} + \cdots \quad \text{(A13)}$$

$$z^{(0)} = z_1 + z_m \quad \text{(A14)}$$

$$z^{(1)} = z_s. \quad \text{(A15)}$$

In the small oscillation limit, the higher order perturbation terms can be ignored. Then, the total force can be separated as the unperturbed and the first order perturbed forces which are given as:

$$F(z) \approx F(z^{(0)}) + F(z^{(1)}) \quad \text{(A16)}$$

$$F(z^{(0)}) = F_1\cos(\omega_1 t) + F_c(z^{(0)}) - \Gamma(z^{(0)})\dot{z}^{(0)} + F_{\text{pif}}^{DC}(z^{(0)}) \quad \text{(A17)}$$

$$F(z^{(1)}) = F_c(z^{(1)}) - \Gamma(z^{(1)})\dot{z}^{(1)} + F_{\text{pif}}^{DC}(z^{(1)})$$

$$+ F_{\text{pif}}^{AC}(z^{(0)})\cos(\omega_m t + \theta_m). \quad \text{(A18)}$$

The integral equations for the unperturbed carrier motion are described as:

$$(k_1 - m\omega_1^2)\frac{A_1}{2} = \frac{1}{T}\int_0^T F(z^{(0)})\sin(\omega_1 t + \theta_1)dt \quad \text{(A19)}$$

$$\frac{b_1\omega_1 A_1}{2} = \frac{1}{T}\int_0^T F(z^{(0)})\cos(\omega_1 t + \theta_1)dt. \quad \text{(A20)}$$

By calculating the above integrals over the period $T = 2\pi p_1/\omega_1 = 2\pi p_s/\omega_s = 2\pi p_m/\omega_m$, the unperturbed solutions

for the carrier motion are found as:

$$(k_1 - \bar{k}_c - m\omega_1^2)A_1 = F_1\sin\theta_1 \quad \text{(A21)}$$

$$(b_1 + \Gamma)\omega_1 A_1 = F_1\cos\theta_1 \quad \text{(A22)}$$

where $\bar{k}_c = \frac{\partial \bar{F}_c}{\partial z}|_{z_c}$ and $\bar{F}_c = F_c + F_{\text{pif}}^{DC}$. By squaring and summing up Eqs. (A21) and (A22), we obtain the unperturbed amplitude of the carrier motion as:

$$A_1 = \frac{F_1}{\sqrt{m^2(\omega_1'^2 - \omega_1^2) + b_1'^2\omega_1^2}} \quad \text{(A23)}$$

with $b'_1 = b_1 + \Gamma(z)$ and $\omega'_1 = \sqrt{(k_1 - \bar{k}_c)/m}$. In order to write the expressions that follow in a more compact form, it is useful to define a transfer function as:

$$G_i(\omega_j) = \frac{1}{\sqrt{m^2(\omega_i'^2 - \omega_j^2)^2 + (b_i'\omega_j)^2}} \quad \text{(A24)}$$

with $b'_i = b_i + \Gamma(z)$ and $\omega'_i = \sqrt{(k_i - \bar{k}_c)/m}$ where $i = 1,2$ and $j = 1,m,s$. Using the transfer function and Eqs. (A21) and (A22), the following relations are found:

$$A_1(\omega_1) = G_1(\omega_1)F_1 \quad \text{(A25)}$$

$$\theta_1(\omega_1) = \tan^{-1}\frac{m(\omega_1'^2 - \omega_1^2)}{b_1'\omega_1} \quad \text{(A26)}$$

$$\bar{k}_c(z_c) = -\frac{F_1}{A_1}\sin\theta_1 + (k_1 - m\omega_1^2) \quad \text{(A27)}$$

$$\Gamma(z_c) = \frac{F_1}{A_1\omega_1}\cos\theta_1 - b_1. \quad \text{(A28)}$$

The sideband motion can be obtained by substituting Eq. (A18) into the equations of motion Eqs. (A3) and (A4). The integral equations for the sideband motion are found as:

$$(k_2 - m\omega_s^2)\frac{A_s}{2} = \frac{1}{T}\int_0^T F(z^{(1)})\sin(\omega_s t + \theta_s)dt \quad \text{(A29)}$$

$$\frac{b_2\omega_s A_s}{2} = \frac{1}{T}\int_0^T F(z^{(1)})\cos(\omega_s t + \theta_s)dt. \quad \text{(A30)}$$

By calculating the above integrals over the period $T = 2\pi p_1/\omega_1 = 2\pi p_s/\omega_s = 2\pi p_m/\omega_m$, the sideband motion is found as:

$$(k_2 - \bar{k}_c - m\omega_s^2)A_s = -\frac{k_{\text{pif}}^{AC}}{2}A_1\cos(\theta_s - (\theta_m - \theta_1)) \quad \text{(A31)}$$

$$(b_2 + \Gamma)\omega_s A_s = \frac{k_{\text{pif}}^{AC}}{2}\sin(\theta_s - (\theta_m - \theta_1)) \quad \text{(A32)}$$

where $k_{\text{pif}}^{AC}(z) = \frac{\partial F_{\text{pif}}}{\partial z}|_{z_c}$. We obtain the sideband motion from Eqs. (A31) and (A32) as:

$$A_s(\omega_s) = G_2(\omega_s)\frac{k_{\text{pif}}^{AC}(z_c)}{2}A_1 \quad \text{(A33)}$$

$$\theta_s(\omega_s) = -\cot^{-1}\frac{m(\omega_2'^2 - \omega_s^2)}{b_2'\omega_m} + \theta_m - \theta_1 \quad \text{(A34)}$$

$$|k_{\text{pif}}^{AC}(z_c)| = \frac{A_s(z_c)}{A_1(z_c)}\frac{2}{G_2(\omega_s)}. \quad \text{(A35)}$$

[1] R. Garcia and R. Perez, Dynamic atomic force microscopy methods, Surf. Sci. Rep. **47**, 197 (2002).

[2] R. Garcia and E. T. Herruzo, The emergence of multifrequency force microscopy, Nat. Nanotech. **7**, 217 (2012).

[3] M. Nonnenmacher, M. P. O'Boyle, and H. K. Wickramasinghe, Kelvin probe force microscopy, Appl. Phys. Lett. **58**, 2921 (1991).

[4] Z. Ma, J. Mu, J. Tang, H. Xue, H. Zhang, C. Xue, J. Liu, and Y. Li, Potential sensitivities in frequency modulation and heterodyne amplitude modulation Kelvin probe force microscopes, Nanoscale Res. Lett. **8**, 532 (2013).

[5] T. Wagner, H. Beyer, P. Reissner, P. Mensch, H. Riel, B. Gotsmann, and A. Stemmer, Kelvin probe force microscopy for local characterization of active nanoelectronic devices, Beilstein J. Nanotechnol. **6**, 2193 (2015).

[6] S. D. Solares, S. An, and C. J. Long, Energy transfer between eigenmodes in multimodal atomic force microscopy, Nanotechnology **25**, 475701 (2014).

[7] M. Damircheli, A. F. Payam, and R. Garcia, Optimization of phase contrast in bimodal amplitude modulation AFM, Beilstein J. Nanotechnol. **6**, 1072 (2015).

[8] I. Rajapaksa, K. Uenal, and H. K. Wickramasinghe, Image force microscopy of molecular resonance: A microscope principle, Appl. Phys. Lett. **97**, 073121 (2010).

[9] I. Rajapaksa, K. Uenal, and H. K. Wickramasinghe, Raman spectroscopy and microscopy based on mechanical force detection, Appl. Phys. Lett. **99**, 161103 (2011).

[10] J. Jahng, J. Brocious, D. A. Fishman, F. Huang, X. Li, V. A. Tamma, H. K. Wickramasinghe, and Eric O. Potma, Gradient and scattering forces in photoinduced force microscopy, Phys. Rev. B **90**, 155417 (2014).

[11] J. Jahng, J. Brocious, D. A. Fishman, S. Yampolsky, D. B. Nowak, F. Huang, V. A. Apkarian, H. K. Wickramasinghe, and E. O. Potma, Ultrafast pump-probe force microscopy with nanoscale resolution, Appl. Phys. Lett. **106**, 083113 (2015).

[12] F. Huang, V. A. Tamma, Z. Mardy, J. Burdett, and H. K. Wickramasinghe, Imaging nanoscale electromagnetic near-field distributions using optical forces, Sci. Rep. **5**, 10610 (2015).

[13] J. Jahng, F. T Ladani, R. M. Khan, and E. O. Potma, Visualizing surface plasmon polaritons by their gradient force, Opt. Lett. **40**, 5058 (2015).

[14] J. Jahng, D. A. Fishman, S. Park, D. B. Nowak, W. A. Morrison, H. K. Wickramasinghe, and E. O. Potma, Linear and nonlinear optical spectroscopy at the nanoscale with photo-induced force microscopy, Acc. Chem. Res. **48**, 2671 (2015).

[15] D. Nowak, W. Morrison, H. K. Wickramasinghe, J. Jahng, E. Potma, L. Wan, R. Ruiz, T. R. Albrecht, K. Schmidt, J. Frommer, D. P. Sanders, and S. Park, Nanoscale chemical imaging by photoinduced force microscopy, Sci. Adv. **2**, e1501571 (2016).

[16] V. A. Tamma, F. Huang, D. Nowak, and H. K. Wickramasinghe, Stimulated Raman spectroscopy and nanoscopy of molecules using near field photon induced forces without resonant electronic enhancement gain, Appl. Phys. Lett. **108**, 233107 (2016).

[17] R. W. Clough and J. Penzien, *Dynamics of Structures* (McGraw-Hill, Singapore, 1993).

[18] M. R. M. Crespo da Silva and C. L. Zaretzky, Non-linear modal coupling in planar and non-planar responses of inextensional beams, Int. J. Non-Linear Mech. **25**, 227 (1990).

[19] C. Dietz, M. Schulze, A. Voss, C. Riesch, and R. W. Stark, Bimodal frequency-modulated atomic force microscopy with small cantilevers, Nanoscale **7**, 1849 (2015).

[20] M. Lee and W. Jhe, General Theory of Amplitude-Modulation Atomic Force Microscopy, Phys. Rev. Lett. **97**, 036104 (2006).

[21] J. R. Lozano and R. Garcia, Theory of phase spectroscopy in bimodal atomic force microscopy, Phys. Rev. B **79**, 014110 (2009).

[22] R. Garcia, C. J. Gomez, N. F. Martinez, S. Patil, C. Dietz, and R. Magerle, Identification of Nanoscale Dissipation Processes by Dynamic Atomic Force Microscopy, Phys. Rev. Lett. **97**, 016103 (2006).

[23] C. J. Gómez and R. Garcia, Determination and simulation of nanoscale energy dissipation processes in amplitude modulation AFM, Ultramicroscopy **110**, 626 (2010).

[24] P. M. Hoffmann, S. Jeffery, J. B. Pethica, H. Ö. Özer and A. Oral, Energy Dissipation in Atomic Force Microscopy and Atomic Loss Processes, Phys. Rev. Lett. **87**, 265502 (2001).

[25] The photoinduced force is driven by a modulated laser beam and contains a DC and AC component, i.e., F_{pif}^{DC} and F_{pif}^{AC}, respectively. Note that because the light has no negative intensity, a fully AC modulated laser beam produces a force of the following form: $F_{\mathrm{pif}} = \frac{1}{2}(F_{\mathrm{pif}}^{DC} + F_{\mathrm{pif}}^{AC}\cos(\omega_m t + \theta_{\mathrm{pif}}))$, where $F_{\mathrm{pif}}^{DC} = F_{\mathrm{pif}}^{AC}$.

[26] R. Garcia and E. T. Herruzo, Force reconstruction from tapping mode force microscopy experiments, Nanotechnology **26**, 185706 (2015).

[27] J. N. Israelachvili, *Intermolecular and Surface Forces* (Academic Press, New York, 1994).

[28] J. E. Sader and S. P. Jarvis, Accurate formulas for interaction force and energy in frequency modulation force spectroscopy, Appl. Phys. Lett. **84**, 1801 (2004).

[29] J. Jahng, F. T. Ladani, R. M. Khan, and E. O. Potma, Photo-induced force for spectroscopic imaging at the nanoscale, Proc. SPIE 9764, Complex Light and Optical Forces **X**, 97641J (2016).

[30] $A_{01} = 10$ nm, $H = 40 \times 10^{-20}$ J, $R = 15$ nm $k_1 = 40$ N/m, $Q_1 = 400$, $\omega_{01} = 2\pi \times 300$ kHz, $k_2 = 1572.5$ N/m, $Q_2 = 600$, $\omega_{02} = 2\pi \times 1.88$ MHz, $\omega_m = 2\pi \times 2.18$ MHz, $\beta = 1 \times 10^{-46}$ Nm^4, and $F_{sc} = 50$ pN.

[31] D. C. Kohlgraf-Owens, S. Sukhov, and A. Dogariu, Optical-force-induced artifacts in scanning probe microscopy, Opt. Lett. **36**, 4758 (2011).

[32] D. C. Kohlgraf-Owens, S. Sukhov, L. Greusard, Y. De Wilde, and A. Dogariu, Optically induced forces in scanning probe, Nanophotonics **3**, 105 (2014).

[33] E. J. Menke, M. A. Thompson, C. Xiang, L. C. Yang, and R. M. Penner, Lithographically patterned nanowire electrodeposition, Nat. Mater. **5**, 914 (2006).

[34] H. Butt and M. Jaschke, Calculation of thermal noise in atomic force microscopy, Nanotechnology **6**, 1 (1995).

[35] A. M. Katzenmeyer, J. Chae, R. Kasica, G. Holland, B. Lahiri, and A. Centrone, Nanoscale Imaging and Spectroscopy of Plasmonic Modes with the PTIR Technique, Adv. Opt. Mater. **2**, 718 (2014).

[36] L. D. Landau and E. M. Lifshitz, *Mechanics* (Academic Press, Oxford, 1976).

[37] W. J. Venstra, H. J. R. Westra, and H. S. J. van der Zant, Q-factor control of a microcantilever by mechanical sideband excitation, Appl. Phys. Lett. **99**, 151904 (2011).

[38] D. Forchheimer, R. Forchheimer, and D. B. Haviland, Improving image contrast and material discrimination with nonlinear response in bimodal atomic force microscopy, Nat. Commun. **6**, 6270 (2015).

[39] D. Platz, E. A. Tholén, D. Pesen, and D. B. Haviland, Intermodulation atomic force microscopy, Appl. Phys. Lett. **92**, 153106 (2008).

[40] W. Melitz, J. Shena, A. C. Kummela, and S. Lee, Kelvin probe force microscopy and its application, Surf. Sci. Rep. **66**, 1 (2011).